

# Stretchable Redox-Active Semiconducting Polymers for High-Performance Organic Electrochemical Transistors

*Yahao Dai, Shilei Dai, Nan Li, Yang Li, Maximilian Moser, Joseph Strzalka, Aleksander Prominski, Youdi Liu, Qingteng Zhang, Songsong Li, Huawei Hu, Wei Liu, Shivani Chatterji, Ping Cheng, Bozhi Tian, Iain McCulloch, Jie Xu, and Sihong Wang\**

Organic electrochemical transistors (OECTs) represent an emerging device platform for next-generation bioelectronics owing to the uniquely high amplification and sensitivity to biological signals. For achieving seamless tissue–electronics interfaces for accurate signal acquisition, skin-like softness and stretchability are essential requirements, but they have not yet been imparted onto high-performance OECTs, largely due to the lack of stretchable redox-active semiconducting polymers. Here, a stretchable semiconductor is reported for OECT devices, namely poly(2-(3,3'-bis(2-(2-methoxyethoxy)ethoxy)-[2,2'-bithiophen]-5)yl thiophene) (p(g2T-T)), which gives exceptional stretchability over 200% strain and 5000 repeated stretching cycles, together with OECT performance on par with the state-of-the-art. Validated by systematic characterizations and comparisons of different polymers, the key design features of this polymer that enable the combination of high stretchability and high OECT performance are a nonlinear backbone architecture, a moderate side-chain density, and a sufficiently high molecular weight. Using this highly stretchable polymer semiconductor, an intrinsically stretchable OECT is fabricated with high normalized transconductance ( $\approx 223 \text{ S cm}^{-1}$ ) and biaxial stretchability up to 100% strain. Furthermore, on-skin electrocardiogram (ECG) recording is demonstrated, which combines built-in amplification and unprecedented skin conformability.

of physiological and mental conditions are of growing interest in clinical and daily healthcare.<sup>[1,2]</sup> Recently, organic electrochemical transistor (OECT)-based biosensors have gained extensive attention<sup>[3,4]</sup> due to their uniquely high amplification,<sup>[5]</sup> and thereby high sensitivity, for detecting low-amplitude signals<sup>[6]</sup> even down to the single-molecule<sup>[7]</sup> or sub-millivolt<sup>[8,9]</sup> levels. Compared to conventional field-effect transistors (FETs), the key difference in OECT lies in the semiconducting channel layers with mixed electronic and ionic transport that allows redox doping/dedoping in electrolyte with extraordinarily high transconductance ( $G_m$ ) to gate modulation.<sup>[5]</sup>

To fully leverage OECTs' advantage in high sensitivity for wearable and implantable biosensing, skin-like softness and stretchability are pivotal<sup>[10,11]</sup> for achieving seamless interfacing with curvilinear skin/tissue surfaces,<sup>[12]</sup> improving biocompatibility and wearing comfort,<sup>[13]</sup> and ultimately realizing high-fidelity signal transduction.<sup>[14]</sup> So far, the reported

successes in developing stretchable OECTs are all based on one type of conjugated polymer as the channel layer: poly(3,4-ethylenedioxythiophene) polystyrene sulfonate (PEDOT:PSS), through strain-engineering,<sup>[15–19]</sup> microstructure-engineering,<sup>[20]</sup>

## 1. Introduction

Wearable and implantable electronics that can intimately integrate with human bodies to provide continuous monitoring

Y. Dai, S. Dai, N. Li, Y. Li, Y. Liu, S. Li, H. Hu, W. Liu, S. Chatterji, P. Cheng, S. Wang  
Pritzker School of Molecular Engineering  
The University of Chicago  
Chicago, IL 60637, USA  
E-mail: sihongwang@uchicago.edu

M. Moser, I. McCulloch  
Department of Chemistry  
University of Oxford  
Oxford OX1 3TA, UK

 The ORCID identification number(s) for the author(s) of this article can be found under <https://doi.org/10.1002/adma.202201178>.

© 2022 The Authors. Advanced Materials published by Wiley-VCH GmbH. This is an open access article under the terms of the Creative Commons Attribution-NonCommercial License, which permits use, distribution and reproduction in any medium, provided the original work is properly cited and is not used for commercial purposes.

DOI: [10.1002/adma.202201178](https://doi.org/10.1002/adma.202201178)

J. Strzalka, Q. Zhang  
X-Ray Science Division  
Argonne National Laboratory  
Lemont, IL 60439, USA

A. Prominski, B. Tian  
Department of Chemistry  
University of Chicago  
Chicago, IL 60637, USA

I. McCulloch  
KAUST Solar Center (KSC)  
King Abdullah University of Science and Technology (KAUST)

Thuwal 23955–6900, Saudi Arabia  
J. Xu, S. Wang  
Nanoscience and Technology Division  
Argonne National Laboratory  
Lemont, IL 60439, USA

or packing-structure engineering.<sup>[21]</sup> However, PEDOT:PSS, as a heavily-doped conjugated polymer, can only allow OECTs to operate under depletion mode, which is not preferred for low power consumption.<sup>[22,23]</sup> In addition, PEDOT:PSS provides just moderate OECT performance that is an order of magnitude lower than the state-of-the-art,<sup>[24,25]</sup> as characterized by the product of the charge-carrier mobility ( $\mu$ ) and volumetric charge-storage capacitance ( $C^*$ ).

More recently, substantial progress has been made in the development of nondoped, redox-active semiconducting polymers (RASPs),<sup>[26,27]</sup> which not only enable OECTs to function in enhancement mode, but also provide largely increased  $[\mu C^*]$ .<sup>[25,28–30]</sup> Compared to the semiconducting polymers designed for organic field-effect transistors (OFETs), for which effective strategies have been reported for imparting stretchability, RASPs are based on different design principles for enabling efficient ion transport and redox doping in aqueous-stable voltage windows.<sup>[31,32]</sup> So far, there has not been any report of stretchable RASPs, not to mention the design principles on the chemical structures and molecular sizes for integrating high stretchability and high OECT performance. This currently stands as the major gap preventing the realization of stretchable OECT-based sensors with high sensitivity and low power consumption.

Here, we report a high-performance stretchable RASP, namely poly(2-(3,3'-bis(2-(2-methoxyethoxy)ethoxy)-[2,2'-bithiophen]-5)yl thiophene) (p(g2T-T)), which shows extraordinary stretchability to 200% strain, and 5000 repeated stretching cycles (to 100% strain). To unravel the design principles for combining high stretchability and high OECT performance on RASPs, we have carried out systematic studies on the effects of chemical structures and molecular weights (MWs). Through combining the stretchable p(g2T-T) with a gold-based stretchable conductor, we also successfully fabricated a fully stretchable OECT (Figure 1a) that, unprecedentedly, has a stretchability of 100% strain, together with a normalized  $G_m$  of 233 S cm<sup>-1</sup>, which is the highest among all the reported stretchable OECT.<sup>[15]</sup> The merit of its high conformability and high sensitivity for the human-interfaced recording of physiological signals was demonstrated through the skin-conformable measurement of electrocardiogram (ECG), which gave superior signal quality with minimal influences from skin deformations.

## 2. Results and Discussion

For creating stretchable RASPs (Figure 1a) with high OECT performance, we reason that the chemical structure should satisfy three requirements: (1) relatively electron-rich backbone for low oxidation voltage in aqueous electrolytes; (2) polar side chains to allow sufficient aqueous swelling for efficient ion transport; (3) moderate backbone planarity for enabling, on one hand, efficient charge delocalization, and on the other hand, effective strain dissipation under stretching.<sup>[33]</sup> These criteria, putting together, led us to the identification of the polymer structure (Figure 1a, namely p(g2T-T)<sup>[28]</sup>) with a polythiophene backbone that has moderate chain flexibility, and polar triethylene-glycol side chains to allow for the penetration of hydrated ions. To achieve efficient intrachain charge transport between

crystalline domains, we synthesized this polymer with a sufficiently high MW ( $M_n = 67.5$  kDa, PDI = 2.15; Figures S1 and S2, Supporting Information).

The stretchability of the p(g2T-T) thin film was tested by stretching on a polydimethylsiloxane (PDMS) substrate to 200% strain (Figure 1b). By optical microscopy and atomic force microscopy (AFM) (Figure 1c), it can be observed that the film maintained crack-free morphology, with a small roughness ( $R_a$ ) of  $2.7 \pm 0.7$  nm. The OECT performance of this polymer during stretching to 200% strain was investigated (Figure 1d) using a typical OECT structure assembled by the soft contact lamination method (Figure S3, Supporting Information). During the stretching parallel to the charge-transport direction, the transfer curves (Figure 1d) and output curves (Figure S4, Supporting Information) of the OECT operation stay nearly unaffected, just with some minor decrease of the peak  $G_m$  from  $\approx 20$  to  $\approx 17.5$  mS (Figure S5, Supporting Information). This should mainly come from the decrease in the film thickness under stretching. Upon releasing, moderate decreases of the on-current and peak  $G_m$  are observed, which are likely due to the deteriorated electrode contact from the microscopic buckling of the p(g2T-T) film (Figure S6, Supporting Information). During the stretching perpendicular to the charge transport, slightly more pronounced decreases of the on-current and peak  $G_m$  are observed (Figures S7 and S8, Supporting Information). For further dissecting the strain's influences on the RASP's intrinsic properties from the device geometry changes, normalized  $G_m$  ( $G_{m,\text{normalized}}$ ) was extracted, which has the following relationships with  $\mu$ ,  $C^*$ , and the threshold voltage ( $V_{\text{th}}$ )

$$G_{m,\text{normalized}} = \mu C^* (V_{\text{gs}} - V_{\text{th}}) \quad (1)$$

Notably, when the strain is parallel to the charge-transport direction, the  $G_{m,\text{normalized}}$  (Figure 1e) steadily increases by 70% upon the application of 200% strain, while in the perpendicular direction the  $G_{m,\text{normalized}}$  gradually decreases to 1/3 of the initial value. To further understand the origin of such strong anisotropy in the responses to the stretching, the strain-induced evolution of  $\mu$  was estimated from the p(g2T-T) film by measuring the hole transient time of the OECT<sup>[34]</sup> (Figure S9, Supporting Information). With an initial value of  $0.93$  cm<sup>-2</sup> V<sup>-1</sup> s<sup>-1</sup>, the changing trends of  $\mu$  agree very well with  $G_{m,\text{normalized}}$  (Figure 1e). On the other hand, the influence of the strain on the redox doping process was evaluated by measuring  $C^*$  from the stretched p(g2T-T) film using electrical impedance spectroscopy (EIS) (Figure S10, Supporting Information) and fitting with a simplified Randle model.<sup>[29]</sup> As shown in Figure 1f, there is only less than 6% change in  $C^*$  during the stretching process. Additionally, the variation of the  $V_{\text{th}}$  is less than 70 mV (Figure 1f), which is consistent with the nearly unshifted oxidation onset voltage ( $V_{\text{ox, onset}}$ ) given by the cyclic voltammetry (CV) measurement (Figure S11, Supporting Information). Taken together, these results reveal that the influence of applied strains on p(g2T-T)'s OECT performance mainly acts on the polymer's  $\mu$ . At the molecular level, we reason that the strain predominately impacts the conformation of polymer chains without causing significant bond rupture, therefore the charge transport shows some dependence on the strain level while the redox capacity is largely maintained constant. The

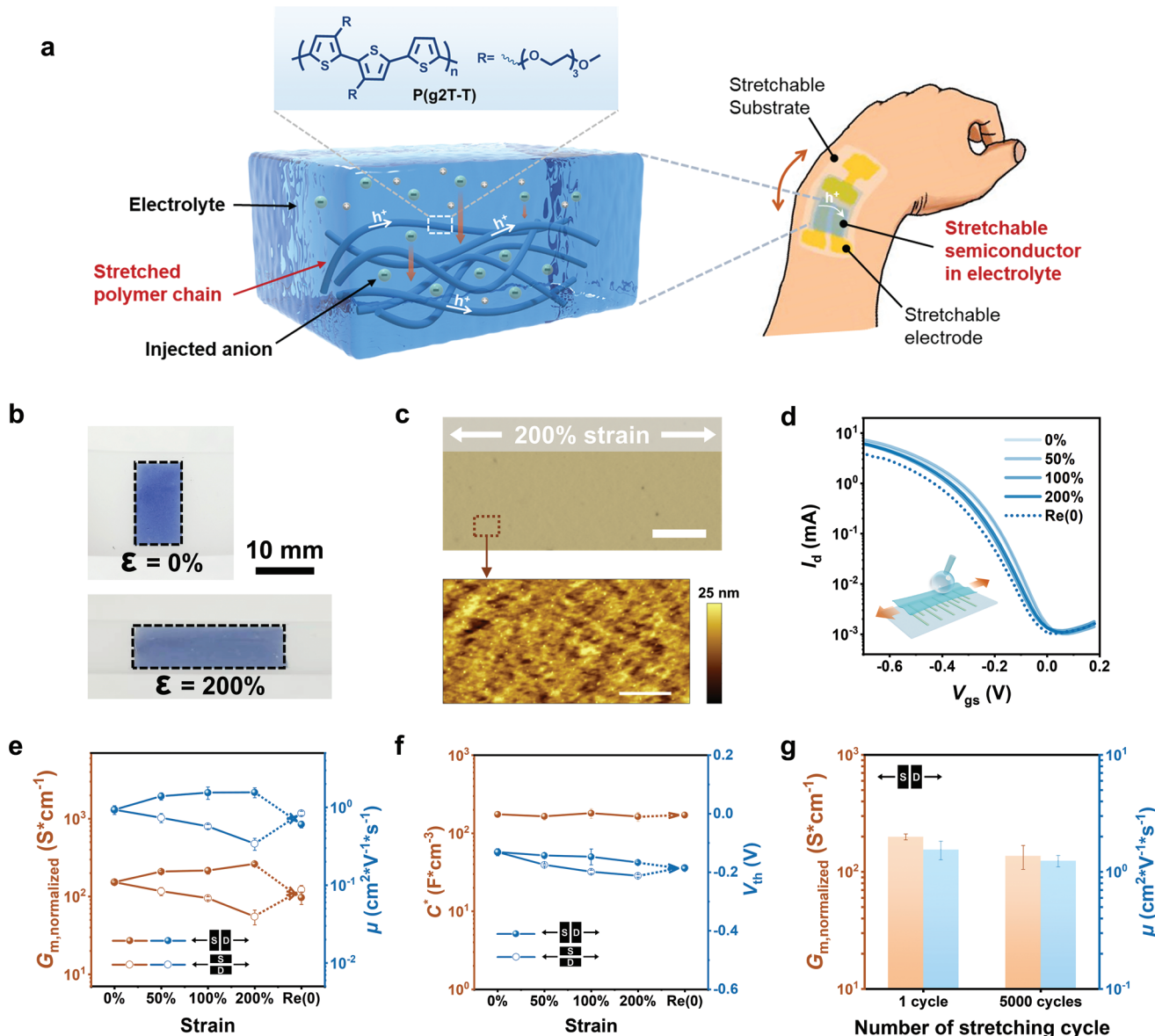


**Figure 1.** Highly stretchable p(g2T-T) as the channel material for OECTs. a) Schematic of the mixed ion and hole transport within a stretched p(g2T-T) film, which can be used to build highly stretchable and wearable OECTs. b) Photographs of a p(g2T-T) film at 0% or 200% strain. c) Optical microscopy image (scale bar: 20  $\mu$ m) and AFM image (scale bar: 1  $\mu$ m) of the p(g2T-T) thin film under 200% strain. d) Transfer curves ( $V_{ds} = -0.6$  V) of the OEET obtained from p(g2T-T) film under different strains ranging from 0% to 200% in parallel to the charge-transport direction. e)  $G_{m,\text{normalized}}$  and  $\mu$  of the stretched p(g2T-T) in OEET devices, which are along two directions: in parallel (filled circles) and in perpendicular (open circles) to the charge-transport direction. f)  $C^*$  and  $V_{th}$  of the p(g2T-T) film under different strains. The  $V_{th}$  was extracted from the transfer curves of OEETs with the stretched p(g2T-T) films. Films were stretched along two directions: in parallel (filled circles) and perpendicular (open circles) to the charge-transport direction.  $C^*$  was calculated from the EIS measurement. g) Changes of the  $G_{m,\text{normalized}}$  and  $\mu$  of the p(g2T-T) film during 5000 repeated stretching cycles to 100% strain. Films were stretched in parallel to the charge-transport direction.

extraordinary stretchability of p(g2T-T) is also reflected by the robustness against cyclic stretching. As shown in Figure 1g and Figure S12 (Supporting Information), the OEET performance is nearly unchanged even after 5000 stretching cycles compared with the single stretching, in both parallel and perpendicular directions.

To understand the strain-dissipation behavior of p(g2T-T) and thereby uncover the reasons for the anisotropic influence of the strain on charge transport, we performed a set of

morphological characterizations to understand the structural evolution of p(g2T-T) film across different length scales. Cross-polarized optical microscopy was first performed to analyze the chain alignment. As shown in Figure 2a and Figure S13 (Supporting Information), stretching to 200% strain changes the p(g2T-T) film from all-angle light extinction to 45° light re-emergence, with respect to the rotation of the polarizer, which indicated the formation of the strong chain alignment from the stretching. To further track the evolution process of such chain

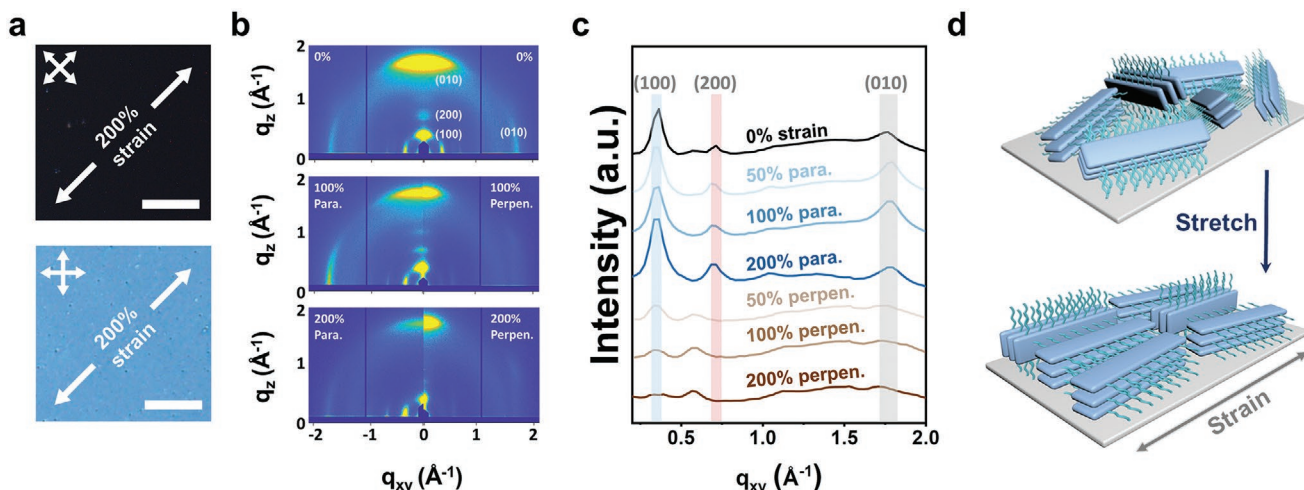


**Figure 2.** Morphological characterizations of a p(g2T-T) film during stretching. a) Cross-polarized optical microscopy images of the stretched p(g2T-T). The orthogonal arrows represent the direction of polarizers. Scale bar: 500  $\mu\text{m}$ . b) GIXD patterns of p(g2T-T) films under 0%, 100%, and 200% strains, with the incident beam both in parallel (on the left) and in perpendicular (on the right) to the strain direction. c) In-plane line cut of the GIXD patterns for p(g2T-T) stretched in both directions from 0% to 200% strain, offset for clarity. d) Schematics showing the rotation and alignment of the crystalline structure under strain.

alignment during stretching, we utilized polarized UV-vis spectroscopy to measure the dichroic ratio (i.e., the ratio between the absorption intensity parallel to the alignment direction and that perpendicular to the alignment direction), which indeed shows the gradual chain alignment during the entire stretching process to 200% strain (Figure S14, Supporting Information). To study the evolution of crystalline packing structures under stretching, we further carried out grazing-incidence X-ray diffraction (GIXD) on strained films (Figure S15, Supporting Information). Initially, the diffraction pattern indicates a mixed packing structure with both face-on and edge-on orientations (Figure 2b). During the stretching to 200% strain, strong anisotropy in the in-plane ( $q_{xy}$ ) diffraction emerges with the incident X-ray beam parallel versus perpendicular to the strain direction. Specifically, higher diffraction intensities from the strain-parallel incidence beam indicate the preferred polymer chain alignment in the strain direction. In addition, from the in-plane 1D linecuts (Figure 2c), it can be observed that under 200% strain the relative intensity of the lamella-packing diffraction (100) to the  $\pi$ - $\pi$  stacking diffraction (010) from strain-parallelled incident beam gets significantly increased, which is likely due to the partial rotation of edge-on packing to face-on packing at large strains (Figure 2d).<sup>[35]</sup> On the molecular level, the effective strain dissipation through the chain reorientation and alignment should originate from both the relatively flexible thiophene backbone and the moderate interchain  $\pi$ - $\pi$  stacking from the asymmetric backbone structure.

To extract the general design principles for stretchable, high-performance RASPs, we further investigate the influences of side-chain density, backbone linearity, and MW. For studying the two chemical-structure factors, we synthesized another polythiophene-based RASP,<sup>[36]</sup> namely poly-[3,3'-bis(2-(2-(2-methoxyethoxy)ethoxy)-2,2'-bithiophene] (p(gT2)) ( $M_n = 71.0$  kDa; PDI = 3.1; Figures S16 and S17, Supporting Information), for comparing both their OECT performance and mechanical properties (Figure 3a). For OECT performance,

the  $[\mu C^*]$  was calculated as the figure-of-merit for the comparison.<sup>[24]</sup> As shown in Figure 3b, the  $[\mu C^*]$  given by p(gT2) is only about half of that from p(g2T-T), which is mainly originated from the difference in  $\mu$ , with their  $C^*$  being similar (Figure S18, Supporting Information). From the GIXD (Figure S19, Supporting Information) and UV-vis results (Figure S20, Supporting Information), the more efficient charge transport in p(g2T-T) can be attributed to the closer  $\pi$ - $\pi$  stacking (3.56  $\text{\AA}$  vs 3.74  $\text{\AA}$  from p(gT2)), and stronger short-range aggregation. We reason that the stronger packing in p(g2T-T) should come from the lower side-chain substitution density.

Next, the stretchability was compared by also stretching a p(gT2) film to 200% strain. As shown in Figure 3c, large cracks were generated on a p(gT2) film, together with a substantially increased surface roughness ( $R_a = 8.3 \pm 1.1$  nm). Such inferior stretchability than p(g2T-T) is also reflected from the change of the dichroic ratio during stretching, which shows that the strain dissipation through chain alignment only lasts to about 150% strain (Figure 3d). When functioning in OECT devices, the lower stretchability of p(gT2) indeed leads to less stable performance (Figure 3e; Figure S21, Supporting Information) against strain than p(g2T-T). Furthermore, the measurement of the elastic moduli of these two polymer films using the buckling method (Figure S22, Supporting Information) also shows that p(gT2) is stiffer than p(g2T-T) by  $\approx 50\%$  (Figure 3f). Structurally, such differences in the mechanical properties can be attributed to the higher relative degree of crystallinity (RDoC) in p(gT2) than p(g2T-T) (Figure 3f), as a result of p(gT2)'s linear backbone structure as compared to the zigzag backbone structure of p(g2T-T). In addition, the measurement of glass-transition temperatures ( $T_g$ 's) from these two polymers (Figure S23, Supporting Information) reveals that p(g2T-T) has higher chain dynamics than p(gT2), which also benefits stretchability. Overall, this set of comparisons shows that the additional unsubstituted thiophene unit in p(g2T-T), which leads to both nonlinear backbone and decreased

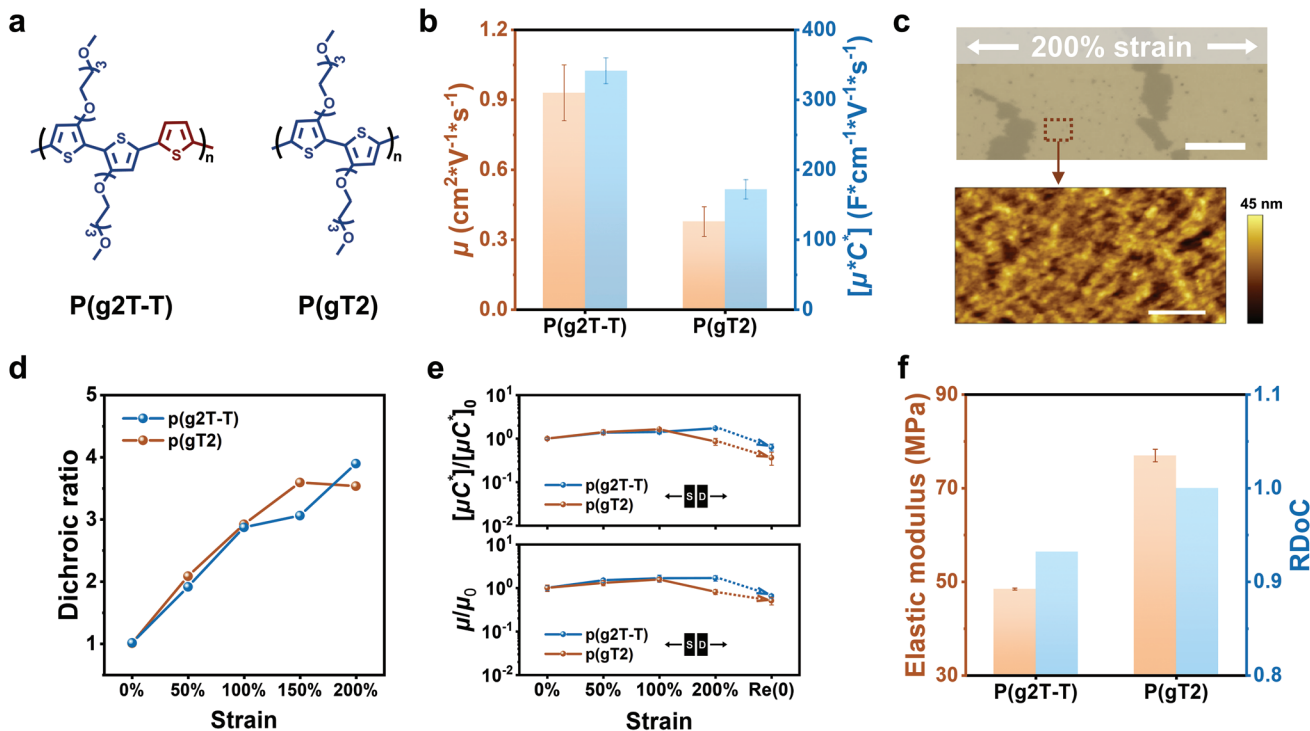


**Figure 3.** Investigation of the influences of the backbone structure and side-chain density. a) Chemical structures of p(g2T-T) and p(gT2). b) OECT performance (i.e.,  $\mu$  and  $[\mu C^*]$ ) comparison of p(g2T-T) and p(gT2). c) Optical microscopy image (scale bar:  $20 \mu\text{m}$ ) and AFM image (scale bar:  $1 \mu\text{m}$ ) of the p(gT2) under 200% strain. d) Changing trends of the calculated dichroic ratios of p(g2T-T) and p(gT2) films during the stretching from 0% to 200% strain. e) OECT performance of p(gT2) and p(g2T-T) films that were stretched in parallel to the charge-transport direction. f) Elastic moduli and RDoC of p(g2T-T) and p(gT2).

side-chain density, could benefit both the OECT performance and stretchability.

Aside from the chemical structures, the influences of a polymer's MW on both the electrical and mechanical properties are systematically studied on p(g2T-T), by synthesizing four evenly distributed MWs in the range of 21–68 kDa (Figure S24 and Table S1, Supporting Information). The  $[\mu C^*]$  of p(g2T-T) shows high dependence on the MW, which mainly reflects MW's influence on  $\mu$  (Figure 4a; Figure S25, Supporting Information). In general, MW acts on the charge-transport property through two aspects working together: higher crystallinity and structural ordering at lower MW, and better tie-chain effect<sup>[37]</sup> at higher MW. For the case of p(g2T-T), the GIXD results (Figure 4b; S26, Supporting Information) and UV-vis measurement (Figure S27, Supporting Information) indeed reveal higher structural ordering at lower MW, and notably, a significant increase for the lowest MW (21 kDa) in this group as indicated by the redshift of the absorption onset. The decreasing trend of  $\mu$  from 21 to 53 kDa suggests that the structural aspect should play the dominating role in the lower MW range. As the MW further increases to 68 kDa, the enhanced tie-chain effect starts to dominate and leads to the increase of the  $\mu$ . On the other hand, MW should influence mechanical stretchability mainly through crystallinity and entanglement density. Through stretching the thin films of p(g2T-T) in these four MWs to 200% strain, the cracks can be observed at 200% strain for the two lower MWs (i.e., 21 and 36 kDa) (Figure 4c), which indicates their lower stretchability (Figures S28–S30, Supporting Information).

It is worth noting that the 21 kDa polymer film has a much higher crack density and smaller crack size compared with the 36 kDa, which could result from the higher modulus of the 21 kDa polymer. Furthermore, this trend of higher stretchability from higher MW is also reflected by the change of these films' OECT performance (i.e.,  $[\mu C^*]$  and  $\mu$  in Figure 4d, and Figure S31, Supporting Information) during stretching to 200% strain, with the 21 kDa MW giving the most severe degradation. Besides being more stretchable, higher MW also makes the polymer softer, as shown by the decrease of the elastic moduli of these p(g2T-T) thin films (Figure 4e; Figure S32, Supporting Information). The structural origin of such influences of MW is verified by the GIXD results, which show a considerable decrease of RDoC from the increase of MW (Figure 4e).

Enabled by the high stretchability from p(g2T-T), we proceed to fabricate fully stretchable OECT devices on PDMS substrates. For the S/D electrodes, we utilized a design of stretchable Au based on vertically grown nanowire morphology<sup>[38]</sup> (Figure S33, Supporting Information), which can provide both the required low resistance ( $\approx 20 \Omega \cdot \text{sq}^{-1}$ ) (Figure S34, Supporting Information) and electrochemical stability for OECT operations. The fabrication of the stretchable OECT was achieved by transferring a p(g2T-T) film onto a PDMS substrate with pre-grown Au electrode patterns. In an aqueous NaCl electrolyte with an Ag/AgCl standard electrode serving as the reference gate (Figure 5a), the fully stretchable OECT can provide ideal switching behavior in the sub-1 V voltage range, with the peak  $G_m$  achieving 4.2 mS (Figure 5b). During the stretching to

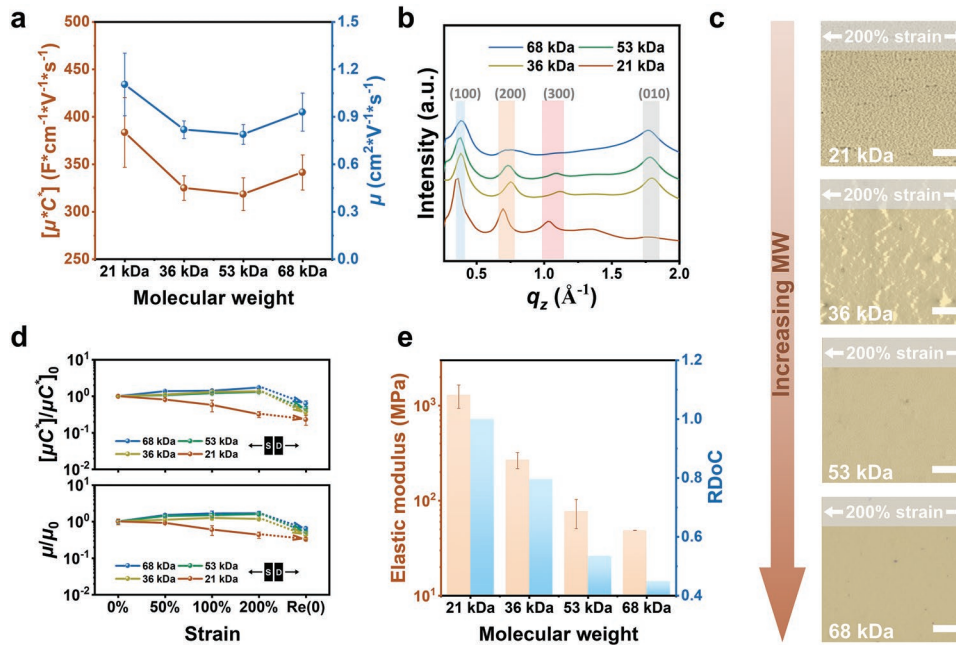


**Figure 4.** Investigation of the influence of MWs on p(g2T-T). a) OECT performance (i.e.,  $\mu$  and  $[\mu C^*]$ ) comparison of p(g2T-T) with different MWs. b) GIXD out-of-plane line cut of the thin films of p(g2T-T) with different MWs, offset for clarity. c) Optical microscopy images of p(g2T-T) thin films with different MWs under 200% strain. Scale bar: 20  $\mu$ m. d) OECT performance of p(g2T-T) films that were stretched in parallel to the charge-transport direction. e) Elastic moduli and RDoC of p(g2T-T) films with different MWs.

100% strain in both directions, the  $G_m$  only displayed minor changes well within one order of magnitude (Figure 5c; Figures S35 and S36, Supporting Information), which should come from the combined effects of strain-induced anisotropy in the p(g2T-T) film and device dimension (i.e., the channel length ( $L$ ) and channel width ( $W$ ) changes. Moreover, the OECT performance is also highly stable during at least 1000 repeated stretching cycles to 100% strain (Figures S37 and S38, Supporting Information). Compared with previously reported fully stretchable OECTs<sup>[15–21]</sup> that are all based on PEDOT:PSS channel layer, our device based on a stretchable semiconducting polymer not only achieved the normalized  $G_m$  70% higher, but also better stretchability in both directions (Figure 5d), together with the enhancement-mode operation that is highly desired for low power consumption (Figure 5d; Table S2, Supporting Information). Besides the great mechanical robustness and electrical performance, the OECT also showed great resistance to high temperature and UV light, which is favored for long-term wearable applications (Figure S39, Supporting Information).

Finally, to demonstrate the applicability of our stretchable OECT for skin-conformable sensing of physiological signals with built-in amplification, we attached our device to the human wrist area for the real-time recording of ECG signals. With the ECG signal applied across the gate and source electrodes of the skin-attached OECT (Figure 5e,f), the drain current as the recording signal provides amplification to the signal through the high  $G_m$  of the OECT device, thereby achieving a much higher signal to noise ratio (SNR) compared to the conventional passive electrode recording. (Figure 5g,h; Figure S40, Supporting Information). Furthermore, the high stretchability and skin conformability of this OECT sensor

can allow stable recording during joint movements that cause stretching on the sensor (Figure 5h). Overall, this demonstration shows the unparalleled merits of our stretchable OECTs enabled by stretchable RASPs for human-integrated sensing with high sensitivity, skin/tissue conformability, and biocompatibility at the same time.

### 3. Conclusion

We have reported a highly stretchable and high-performance redox-active semiconducting polymer (RASP), namely p(g2T-T), for the development of stretchable OECT-based sensors. The p(g2T-T) gives extraordinary stretchability to 200% strain, without any crack formation or degradation in its OECT performance that is on par with the state-of-the-art. In-depth structural characterizations reveal that the high stretchability of p(g2T-T) comes from the effective strain dissipation through segmental polymer chain reorientation during stretching. On the general level for the design of stretchable, high-performance RASPs, our further systematic studies have suggested that nonlinear backbone architecture, relatively low side-chain density, and a higher molecular weight could be beneficial design factors. By incorporating the highly stretchable p(g2T-T) film with other stretchable components, intrinsically stretchable OECTs were fabricated, achieving a record-high normalized  $G_m$  ( $\approx 233$  S cm<sup>-1</sup>) and high stretchability of 100% strain, together with the realization of enhancement-mode operation. For demonstrating the unparalleled merits of such stretchable OECTs for human-integrated sensing, our device with great skin conformability successfully served as a wearable sensor for the real-time recording of ECG signals, which achieved both a high

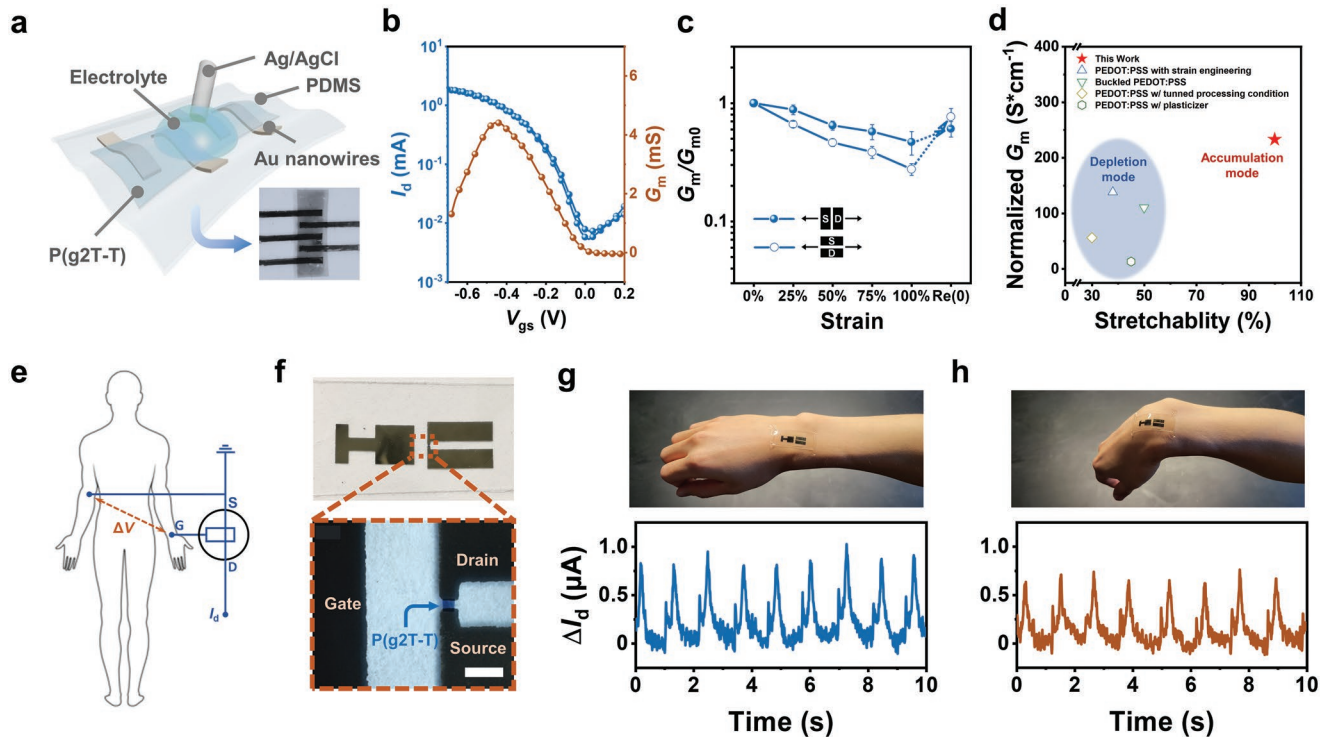


**Figure 5.** P(g2T-T) based intrinsically stretchable OECT, and its function as a wearable ECG sensor. a) Schematic showing the structure of the intrinsically stretchable OECT. b) Transfer curve and  $G_m$  of the intrinsically stretchable OECT at the 0% strain. c) Changes of  $G_m$  of the stretched OECT, which are along two directions: parallel (filled circles) and perpendicular (open circles) to the charge-transport direction. d) Comparisons of our stretchable OECT with previously reported stretchable OECTs that are all based on PEDOT:PSS as the channel layer.<sup>[15,18,20,21]</sup> e) Schematic showing the circuit diagram for the use of the intrinsically stretchable OECT for on-body ECG recording. f) Photograph of the OECT for the ECG test and a zoomed-in optical microscopy image showing the device structure. Scale bar: 500  $\mu$ m. g,h) Photographs showing the conformable attachment of the OECT on the wrist without (g) and with (h) bending, and the corresponding ECG signals acquired from the human body. The gate and source electrodes were connected to commercial gel electrodes that were adhered to the skin for acquiring the ECG signals from the human body.

SNR and stability under skin deformation. This work makes a major step in the development of stretchable polymer semiconductors for leveraging the high-sensitivity advantage of OECTs for skin/tissue-like wearable and implantable biosensing. In pursuit of stretchable OECT-based biosensors for practical applications, future efforts are needed for improving long-term operational stability, high-resolution integration, sensing specificity, and bio/immune-compatibility.

## Supporting Information

Supporting Information is available from the Wiley Online Library or from the author.

## Acknowledgements

Y.D. and S.D. contributed equally to this work. This work is supported by the US Office of Naval Research (N00014-21-1-2266) and a start-up fund from the University of Chicago. J.X. acknowledges the Center for Nanoscale Materials, a US Department of Energy Office of Science User Facility and supported by the US Department of Energy Office of Science, under contract DE-AC02-06CH11357. This research used resources of the Advanced Photon Source, a US Department of Energy Office of Science User Facility, operated for the Department of Energy Office of Science

by Argonne National Laboratory under contract DE-AC02-06CH11357. All the experiments involving human subjects were approved by the University of Chicago Biological Sciences Division/University of Chicago Medical Center Institutional Review Boards, with the assigned study/project number of IRB20-1412; and written informed consent was obtained from all participants.

Note: The figures were reset in higher quality on June 9, 2022, after initial publication online.

## Conflict of Interest

The authors declare no conflict of interest.

## Data Availability Statement

The data that support the findings of this study are available from the corresponding author upon reasonable request.

## Keywords

organic electrochemical transistors, redox-active polymer semiconductors, stretchable electronics

Received: February 5, 2022

Revised: April 10, 2022

Published online: May 2, 2022

- [1] J. Kim, A. S. Campbell, B. E.-F. de Ávila, J. Wang, *Nat. Biotechnol.* **2019**, *37*, 389.
- [2] T. R. Ray, J. Choi, A. J. Bandodkar, S. Krishnan, P. Gutruf, L. Tian, R. Ghaffari, J. A. Rogers, *Chem. Rev.* **2019**, *119*, 5461.
- [3] L. Bai, C. Elósegui, W. Li, P. Yu, J. Fei, L. Mao, *Front. Chem.* **2019**, *7*, 313.
- [4] M. Sophocleous, L. Contat-Rodrigo, E. Garcia-Breijo, J. Georgiou, *IEEE Sens. J.* **2021**, *21*, 3977.
- [5] J. Rivnay, S. Inal, A. Salleo, R. M. Owens, M. Berggren, G. G. Malliaras, *Nat. Rev. Mater.* **2018**, *3*, 17086.
- [6] N. Wang, A. Yang, Y. Fu, Y. Li, F. Yan, *Acc. Chem. Res.* **2019**, *52*, 277.
- [7] K. Guo, S. Wustoni, A. Koklu, E. Díaz-Galicia, M. Moser, A. Hama, A. A. Alqahtani, A. N. Ahmad, F. S. Alhamlan, M. Shuaib, A. Pain, I. McCulloch, S. T. Arold, R. Grünberg, S. Inal, *Nat. Biomed. Eng.* **2021**, *5*, 666.
- [8] C. Cea, G. D. Spyropoulos, P. Jastrzebska-Perfect, J. J. Ferrero, J. N. Gelinas, D. Khodagholy, *Nat. Mater.* **2020**, *19*, 679.
- [9] P. Leleux, J. Rivnay, T. Lonjaret, J. Badier, C. Bénar, T. Hervé, P. Chauvel, G. G. Malliaras, *Adv. Healthcare Mater.* **2015**, *4*, 142.
- [10] Y. Fang, X. Yang, Y. Lin, J. Shi, A. Prominski, C. Clayton, E. Ostroff, B. Tian, *Chem. Rev.* **2022**, *122*, 5233.
- [11] Y. Li, N. Li, N. D. Oliveira, S. Wang, *Matter* **2021**, *4*, 1125.
- [12] Y. Liu, J. Liu, S. Chen, T. Lei, Y. Kim, S. Niu, H. Wang, X. Wang, A. M. Foudeh, J. Tok, Z. Bao, *Nat. Biomed. Eng.* **2019**, *3*, 58.
- [13] S. Wang, J. Xu, W. Wang, G.-J. N. Wang, R. Rastak, F. Molina-Lopez, J. W. Chung, S. Niu, V. R. Feig, J. Lopez, T. Lei, S.-K. Kwon, Y. Kim, A. M. Foudeh, A. Ehrlich, A. Gasperini, Y. Yun, B. Murmann, J. B.-H. Tok, Z. Bao, *Nature* **2018**, *555*, 83.
- [14] I. R. Minev, P. Musienko, A. Hirsch, Q. Barraud, N. Wenger, E. M. Moraud, J. Gandar, M. Capogrosso, T. Milekovic, L. Asboth, R. F. Torres, N. Vachicouras, Q. Liu, N. Pavlova, S. Duis, A. Larmagnac, J. Vörös, S. Micera, Z. Suo, G. Courtine, S. P. Lacour, *Science* **2015**, *347*, 159.
- [15] B. Marchiori, R. Delattre, S. Hannah, S. Blayac, M. Ramuz, *Sci. Rep.* **2018**, *8*, 8477.
- [16] W. Lee, S. Kobayashi, M. Nagase, Y. Jimbo, I. Saito, Y. Inoue, T. Yambe, M. Sekino, G. G. Malliaras, T. Yokota, M. Tanaka, T. Someya, *Sci. Adv.* **2018**, *4*, eaau2426.
- [17] N. Matsuhisa, Y. Jiang, Z. Liu, G. Chen, C. Wan, Y. Kim, J. Kang, H. Tran, H. Wu, I. You, Z. Bao, X. Chen, *Adv. Electron. Mater.* **2019**, *5*, 1900347.
- [18] S. Zhang, E. Hubis, G. Tomasello, G. Soliveri, P. Kumar, F. Cicoria, *Chem. Mater.* **2017**, *29*, 3126.
- [19] Y. Li, N. Wang, A. Yang, H. Ling, F. Yan, *Adv. Electron. Mater.* **2019**, *5*, 1900566.
- [20] Y. Li, S. Zhang, X. Li, V. R. N. Unnava, F. Cicoria, *Flexible Printed Electron.* **2019**, *4*, 044004.
- [21] S. Zhang, Y. Li, G. Tomasello, M. Anthonisen, X. Li, M. Mazzeo, A. Genco, P. Grutter, F. Cicoria, *Adv. Electron. Mater.* **2019**, *5*, 1900191.
- [22] S. T. Keene, T. P. A. Pol, D. Zakhidov, C. H. L. Weijtens, R. A. J. Janssen, A. Salleo, Y. Burgt, *Adv. Mater.* **2020**, *32*, 2000270.
- [23] A. Koklu, S. Wustoni, V.-E. Musteata, D. Ohayon, M. Moser, I. McCulloch, S. P. Nunes, S. Inal, *ACS Nano* **2021**, *15*, 8130.
- [24] S. Inal, G. G. Malliaras, J. Rivnay, *Nat. Commun.* **2017**, *8*, 1767.
- [25] M. Moser, T. C. Hidalgo, J. Surgailis, J. Gladisch, S. Ghosh, R. Sheelamanthula, Q. Thiburce, A. Giovannitti, A. Salleo, N. Gasparini, A. Wadsworth, I. Zozoulenko, M. Berggren, E. Stavrinidou, S. Inal, I. McCulloch, *Adv. Mater.* **2020**, *32*, 2002748.
- [26] B. D. Paulsen, K. Tybrandt, E. Stavrinidou, J. Rivnay, *Nat. Mater.* **2019**, *19*, 13.
- [27] J. H. Kim, S. Kim, G. Kim, M. Yoon, *Macromol. Biosci.* **2020**, *20*, 2000211.
- [28] C. B. Nielsen, A. Giovannitti, D.-T. Sbircea, E. Bandiello, M. R. Niazi, D. A. Hanifi, M. Sessolo, A. Amassian, G. G. Malliaras, J. Rivnay, I. McCulloch, *J. Am. Chem. Soc.* **2016**, *138*, 10252.
- [29] A. Giovannitti, D.-T. Sbircea, S. Inal, C. B. Nielsen, E. Bandiello, D. A. Hanifi, M. Sessolo, G. G. Malliaras, I. McCulloch, J. Rivnay, *Proc. Natl. Acad. Sci.* **2016**, *113*, 12017.
- [30] R. K. Hallani, B. D. Paulsen, A. J. Petty, R. Sheelamanthula, M. Moser, K. J. Thorley, W. Sohn, R. B. Rashid, A. Savva, S. Moro, J. P. Parker, O. Drury, M. Alsufyani, M. Neophytou, J. Kosco, S. Inal, G. Costantini, J. Rivnay, I. McCulloch, *J. Am. Chem. Soc.* **2021**, *143*, 11007.
- [31] E. Zeglio, O. Inganäs, *Adv. Mater.* **2018**, *30*, 1800941.
- [32] M. Moser, J. F. Ponder, A. Wadsworth, A. Giovannitti, I. McCulloch, *Adv. Funct. Mater.* **2019**, *29*, 1807033.
- [33] Y. Dai, H. Hu, M. Wang, J. Xu, S. Wang, *Nat. Electron.* **2021**, *4*, 17.
- [34] D. Bernards, G. Malliaras, *Adv. Funct. Mater.* **2007**, *17*, 3538.
- [35] B. O'Connor, J. R. Kline, B. R. Conrad, L. J. Richter, D. Gundlach, M. F. Toney, D. M. DeLongchamp, *Adv. Funct. Mater.* **2011**, *21*, 3697.
- [36] D. Moia, A. Giovannitti, A. A. Szumska, I. P. Maria, E. Rezasoltani, M. Sachs, M. Schnurr, P. R. F. Barnes, I. McCulloch, J. Nelson, *Energy Environ. Sci.* **2019**, *12*, 1349.
- [37] G. N. Wang, A. Gasperini, Z. Bao, *Adv. Electron. Mater.* **2018**, *4*, 1700429.
- [38] B. Zhu, S. Gong, F. Lin, Y. Wang, Y. Ling, T. An, W. Cheng, *Adv. Electron. Mater.* **2019**, *5*, 1800509.